Journal of Materials Chemistry C

ROYAL SOCIETY OF CHEMISTRY

PAPER

View Article Online
View Journal | View Issue

Cite this: J. Mater. Chem. C, 2021, 9, 9539

A high-temperature quantum anomalous Hall effect in electride gadolinium monohalides†

Chen Chen, [abc] Le Fang, [ab] Guodong Zhao, [ab] Xingen Liu, [ab] Jian Wang, [d] Lee A. Burton, [a] Yunwei Zhang *[e] and Wei Ren *[ab]

Received 1st April 2021,
Accepted 16th June 2021

DOI: 10.1039/d1tc01513c

rsc.li/materials-c

Electrides, with interstitial electrons loosely trapped in lattice voids behaving as anions, are favorable for achieving band inversions required for topological phases. In this paper, we predict that the quantum anomalous Hall effect (QAHE) with either in-plane or out-of-plane magnetization can be realized in gadolinium monohalides GdX (X = F, Cl, Br, and I), a new class of two-dimensional electrides. The spin polarization of interstitial electrons contributes to the ferromagnetism and stabilizes the crystal structure. Our calculations demonstrate that monolayer GdX are intrinsic QAHE insulators with in-plane magnetization and have band gaps up to 48.6 meV. Furthermore, we show that an external magnetic field can be used to realize the QAHE with out-of-plane magnetization, such as in monolayer GdI with the largest band gap of 84.3 meV among all halides considered in this work. The estimated Curie temperatures of GdX are about 510–650 K, which is above room temperature. Our studies reveal that the GdX electrides provide an attractive platform for exploring tunable, large-gap QAHE and open up opportunities to design new high-temperature quantum devices.

Introduction

Electrides are intrinsic electron-rich materials, in which some electrons are trapped in the interstitials of a lattice, playing the role of anions.[1–3] These trapped interstitial electrons are weakly bound to the positively charged lattice framework and form unique interstitial energy bands around the Fermi level, which dominate the electronic and magnetic properties. Although the number of confirmed electrides is limited,[4–8] electride systems can have many intriguing properties, including low work function,[9] high carrier mobility,[5] high catalytic activity,[10] ferromagnetism[8] and superconductivity.[11,12] Recently, it has been proposed that the interstitial electrons in electrides unshared by any atomic orbital are also favorable for achieving band inversion for topological phases.[13,14] A similar scenario of electron distribution has been reported in conventional topological materials composed of heavy elements, where the key to band inversion is hybridized orbitals centered away from any individual atoms.[15,16] Indeed, various types of topological phases were predicted in electrides, *e.g.*, nodal line semimetal in Y_2C and Rb_3O,[17] a topological insulator in Sc_2C, the quantum spin Hall phase in HfBr and the quantum anomalous Hall effect (QAHE) in monolayer LaCl.[13]

Among all these topological phenomena, the QAHE induced by spontaneous magnetization without an extrinsic magnetic field has been particularly attractive for its robust edge state against impurity scattering. Since 1988, when the QAHE was proposed in a two-dimensional (2D) honeycomb model,[18] great efforts have been devoted to explore new QAHE candidates for dissipation-less quantum electronics. Early theoretical studies predicted that many materials can host the QAHE[19–21] and have led to the experimental observation of the QAHE in graphene/boron nitride heterostructures[22] and Cr-doped $(Bi, Sb)_2Te_3$.[23] However, it has long been thought that the QAHE can only be induced by an out-of-plane magnetic field, similar to the observation of the quantum Hall effect in a perpendicular magnetic field.[24] It is only recently that the QAHE with in-plane magnetization was proposed in several models, *e.g.*, magnetically doped Bi_2Te_3 thin films,[25] bulk hexagonal lattices,[26] and one real material of monolayer LaCl with a global band gap of 4 meV.[27] Unfortunately, experiments to realize this QAHE state in LaCl with such a small band gap are very challenging. Electrides offer an alternative, new platform for observing various topological phases, in which we can explore a large-gap QAHE with in-plane magnetization for both fundamental understanding of the exotic interstitial electrons and practical applications of high-temperature quantum devices.

[a] International Center for Quantum and Molecular Structures, Materials Genome Institute, Physics Department, Shanghai University, Shanghai 200444, China. E-mail: renwei@shu.edu.cn
[b] Shanghai Key Laboratory of High Temperature Superconductors and State Key Laboratory of Advanced Special Steel, Shanghai University, Shanghai 200444, China
[c] Fritz-Haber-Institut der Max-Planck-Gesellschaft, Faradayweg 4-6, 14195 Berlin-Dahlem, Germany
[d] College of Physics and Optoelectronic Engineering, Shenzhen University, Shenzhen, Guangdong, China
[e] Cavendish Laboratory, University of Cambridge, Cambridge CB3 0HE, UK. E-mail: yz618@cam.ac.uk

† Electronic supplementary information (ESI) available. See DOI: 10.1039/d1tc01513c

In this work, we predict through first-principles calculations that a new class of 2D electrides GdX (X = F, Cl, Br, and I) can form monolayers that are intrinsic QAHE insulators with in-plane magnetization. By counting the formal charges of Gd and halogen X elements, we show that GdX are intrinsic electron-rich materials with excess electrons (two excess electrons per formula unit) confined in 2D interlayer regions between two Gd^{3+} sheets. Our calculations confirm that the materials of monolayer GdX[28] can be easily exfoliated from the bulk materials and have nontrivial global band gaps of up to 48.6 meV, because of the strong spin–orbit coupling (SOC). Ferromagnetism (FM) is induced by the spin polarization of interstitial electrons. Notably, the energy difference between FM states with in-plane and out-of-plane magnetization is small ($\sim$0.1 meV f.u.$^{-1}$), suggesting that the QAHE with out-of-plane magnetization can be realized experimentally by applying an external magnetic field. We also find that when the direction of magnetization switches to out-of-plane, a large SOC band gap of 84.3 meV can be obtained in monolayer GdI, which is a comfortable value compared to the value around 100 meV reported in all known QAHE systems.[29–31] Monte Carlo simulations demonstrate that GdX have above room temperature FM, with Curie temperatures of 510–650 K, suggesting great potential for practical applications.

Methods

The first-principles calculations were carried out based on density functional theory (DFT) with the Perdew–Burke–Ernzerhof (PBE) exchange correlation functional as implemented in the Vienna ab initio Simulation Package (VASP).[32,33] The all-electron projector-augmented wave (PAW)[34] method was adopted, where $4f^{7}5d^{6}6s^{2}$, and p orbital electrons are treated as valence electrons for Gd, and X (X = F, Cl, Br, and I) atoms, respectively. We included the van der Waals (vdW) interactions based on the vdW-D3 method in the calculations of GdX systems.[33,35] The modified Becke Johnson (mBJ)[36] exchange potential was applied to correct the band gaps obtained by using the PBE functional. The DFT plus Hubbard correction (DFT+U) was used to deal with the *f* electrons in Gd elements, and the Hubbard *U* value of 6.0 eV was adopted according to the previous work.[28] For all calculations in this paper, the plane-wave energy cutoff was set to 600 eV, and a Monkhorst–Pack *k*-point mesh of 9 × 9 × 1 was used. Structural relaxations were performed with energy and forces converged to 10^{-6} eV and 0.01 eV Å^{-1}, respectively. A vacuum space of 20 Å was included to prevent interaction between two adjacent monolayers. The calculation of the phonon band structure was done using the FHI-aims software package,[37–39] which is a complete electronic structure code with all potential energy. The Curie temperature of GdX was estimated by Monte Carlo (MC) simulations,[40] see the ESI for more details.

Results and discussion

Crystal structure and magnetic configurations

Experimentally, GdX (X = F, Cl, Br, and I)[41–45] have a layered $R\bar{3}m$ structure with an ABCBA-type stacking pattern along the z direction (A, B, and C are X^{-} sheets, Gd^{3+} sheets, and anionic electron layers, respectively), as shown in Fig. 1(a). The structural information of GdX is listed in Table 1. Both Gd and X atoms form a trigonal arrangement in their sheets. By counting the formal charges of Gd and X elements as +3 and −1, respectively, GdX contain two intrinsic excess electrons per formula unit (f.u.). As shown in Fig. 1(a) and (b), the electron localization function (ELF) calculations of bulk and monolayer GdCl demonstrate that the excess electrons are confined in the 2D interlayer regions between two adjacent Gd^{3+} sheets, characterizing them to be 2D electrides as reported in its isoelectronic system LaCl.[6] We calculate the exfoliation energy of monolayer GdCl as the representative of GdX in a five-layer slab model, as shown in Fig. 1(d). The converged exfoliation energy is $\sim$7.2 meV Å^{-2}, which is lower than that of LaCl ($\sim$15 meV Å^{-2}),[27] H-MoS_2 ($\sim$18 meV Å^{-2})[46] and graphene ($\sim$21 meV Å^{-2}), indicating that the monolayer GdX can be obtained by mechanical exfoliation.

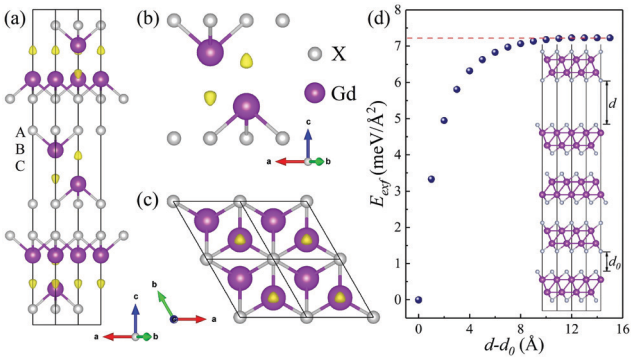

Fig. 1 Crystal structure information of electrides GdX. (a) Electron localization function (ELF) of bulk (a) and monolayer (b) GdX with an isosurface around 0.78. The purple and gray spheres represent the Gd and X atoms, respectively. The yellow parts between two adjacent Gd^{3+} layers in (a) and (b) represent the localized regions for interstitial electrons. (c) Top view of Gd and X sheets in which Gd and X atoms form a buckled honeycomb lattice. (d) The calculated exfoliation energy of monolayer GdCl as the representative of GdX in a five-layer slab model. The inset shows the side view of the slab model with the interlayer distance of d_0. d is the distance between the exfoliated layer and bulk structure.

Next, we performed calculations to explore the magnetic ground state of GdX. Considering that the properties of bulk GdX are similar to that of monolayer GdX, we only discuss the results of monolayer GdCl as the representative of GdX in the following (see more details of bulk and monolayer GdX in the ESI†). We calculate the total energies of different magnetic configurations for monolayer GdCl, including FM magnetization and three anti-ferromagnetic (AFM) configurations, as shown in Fig. S1 in the ESI.† These total energies are summarized in Table S2 in the ESI.† The results show that the monolayer GdCl prefers a FM ground state, with an energy that is lower by 0.06 eV f.u.$^{-1}$, 0.11 eV f.u.$^{-1}$, and 0.20 eV f.u.$^{-1}$ than Néel, zigzag, and stripy type AFM configurations, respectively. The FM ground state of monolayer GdCl is robust, and not affected by the value of Hubbard U and external strain, see more details in Table S3 and S4 in the ESI.† Notably, we find that the FM state with in-plane magnetization has the lowest energy, consistent with the results reported in

Table 1 The lattice constant (Å), thickness (Å), magnetic moments of interstitial electrons (μ_B) and total magnetic moment (μ_B), global band gap (meV) for in-plane and out-of-plane magnetizations, and Curie temperature T_C (*K*) of monolayer GdX (X = F, Cl, Br, and I). All band gaps are corrected by the mBJ method. The details of bulk GdX are listed in Table S1 in the ESI

System	Lattice constant (Å)	Thickness (Å)	Magnetic (μ_B)		Band gap (meV)		T_C (*K*)
			Interstitial electrons	Total	In-plane	Out-of-plane	
GdF	3.587	5.273	1.012	7.442	16.7	20.9	650
GdCl	3.745	6.289	0.914	7.395	30.3	45.7	510
GdBr	3.813	6.612	0.913	7.387	42.6	58.3	530
GdI	3.947	6.985	0.519	7.369	48.6	84.3	560

bulk GdX (as listed in Table S5 in the ESI†).[28] The energy difference between these two FM states is 0.10 meV f.u.$^{-1}$, comparable to that of 0.15 meV f.u.$^{-1}$ in monolayer LaCl.[27] However, the magnetic anisotropy energy is on the order of 0.001 meV, which is indistinguishable for in-plane magnetization with different angles, indicating monolayer GdCl is a soft magnetic material with an easy magnetization axis in the *xoy* plane. It's experimentally feasible to further stabilize the FM state with such small magnetic anisotropy energy by introducing a weak magnetic field.[27]

As shown in Fig. 2(a), the spin polarization effect splits the peaks for the density of states in monolayer GdCl at the Fermi level (E_F) into majority and minority spin states by around 1.9 eV, stabilizing the FM state. This mechanism is known as Stoner-type magnetic instability,[47] which has been reported in several high-pressure[48] and 2D electrides.[8,49] In addition, the spin polarization has a very large impact on the phonon spectrum of monolayer GdCl as shown in Fig. 2(c). The phonon spectrum without spin-polarized calculation has several imaginary modes, while the one with spin-polarized calculation show well-behaved phonon dispersion relations with positive frequencies. The spin density of FM monolayer GdCl is shown in Fig. 2(b). We note that the spin-polarized charge density is concentrated at the interstitial sites localized by excess electrons and Gd atomic sites, while the spin polarization at the Cl atomic sites is small. The magnetic moments of interstitial electrons and Gd atoms are 0.914 μ_B and 7.418 μ_B, respectively, which indicates that the spin polarization of these exotic excess electrons confined between Gd^{3+} sheets play an important role in the FM state. The details of magnetic moments of monolayer and bulk GdX are listed in Table 1 and Table S1 in the ESI,† respectively.

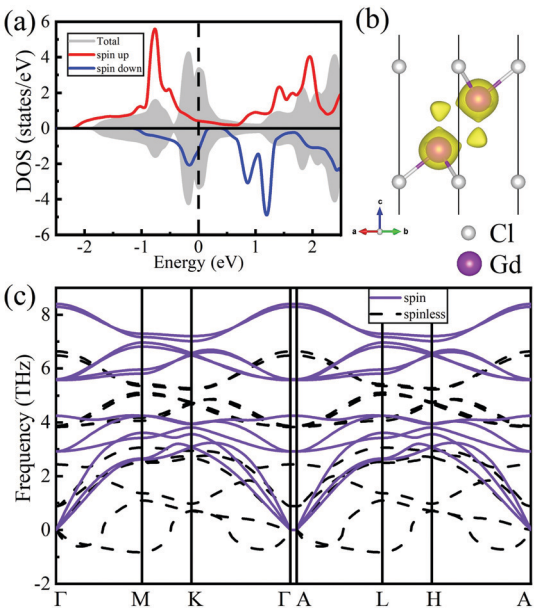

Fig. 2 A Stoner-type instability toward FM in GdCl. (a) Density of state of monolayer GdCl for the paramagnetic state (grey shadow) and FM state with in-plane magnetization (red and blue for majority and minority spin states, respectively). Fermi level (E_F) is shown as a vertical dashed line. (b) Spin density (yellow) of monolayer GdCl with an isosurface of 0.011. The purple and gray spheres represent the Gd and Cl atoms, respectively. (c) Phonon spectra of GdCl from calculations with and without spin-polarized consideration are shown as solid and dashed lines, respectively.

Quantum anomalous Hall effect with in-plane magnetization

Band structures with/without the considerations of SOC for in-plane magnetization have been calculated to explore the electronic property of monolayer GdCl. As shown in Fig. 3(a), the band structure without SOC is spin-polarized along the *K*–Γ–*M*–*K* path in the Brillouin zone. The projected band structure (Fig. S2 in the ESI†) shows that the energy bands near the Fermi level are mainly the Gd 5d (*i.e.* d_{xy}, d_{yz} and d_{z^2}) orbitals. The large intrinsic SOC effect of Gd 5d orbitals is responsible for the origin of topological properties. Two inverted bands with

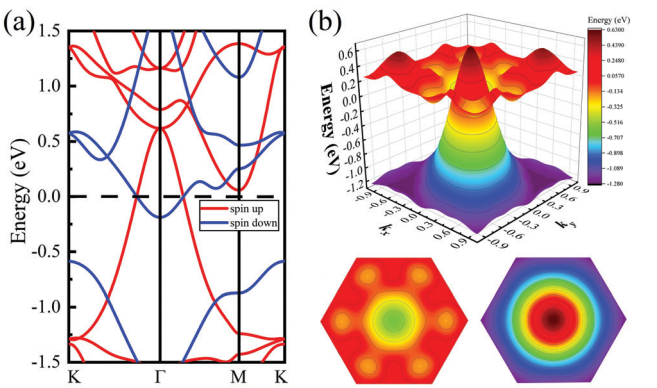

Fig. 3 Electronic properties of monolayer GdCl. (a) Spin-polarized ferromagnetic band structure without spin orbital coupling (SOC). The red (blue) lines represent the majority- (minority-) spin states, the black dashed line at 0 eV indicates the E_F. (b) The top panel is the 3D band structure in the *xoy* plane without the consideration of SOC. The bottom two panels are the top and bottom views of the 3D band structure.

opposite spin states cross at the E_F that forms a nodal line circled around the Γ point, demonstrating a 2D nodal-line semimetal. The nodal line can also be clearly seen in Fig. 3(b), the three-dimensional (3D) band structure where two funnel-shaped electronic bands intersect each other near the Fermi surface. Monolayer GdCl has three mirror planes shown in Fig. 4(a), which are along Γ–M, Γ–M' and Γ–M'', respectively. However, the mirror symmetry can be conserved only when the mirror plane is perpendicular to the direction of magnetization.[27] In monolayer GdCl, the FM order with in-plane magnetization breaks the mirror symmetry with respect to the *xoy* plane (along the Γ–M path). The conserved mirror symmetries with respect to *yoz* (Γ–M') and *xoz* (Γ–M'') planes guarantee twelve twofold degenerate band crossings along the nodal line, shown as red dots in Fig. 4(a). Interestingly, the band gap opening at the nodal line in monolayer GdCl will induce several QAHE phases, as will be discussed below.

By including the SOC effect, each pair of degenerate band crossings (red dots in Fig. 4(a)) decay into two Weyl nodes and a band gap is opened at the nodal-line around the Γ point for in-plane magnetization, as shown in Fig. 4(b). It is worth noting that the band gap of monolayer GdCl depends on the direction of magnetization. We map out the band gap in the three mirror planes (along Γ–M, Γ–M' and Γ–M'' paths) at different spin angles (θ) for in-plane magnetization, as shown in Fig. 4(c). The θ-dependent band gaps for out-of-plane magnetization are shown in Fig. S3 in the ESI.† In Fig. 4(c), the direction of in-plane magnetization along $\theta = 0°$, 60° and 120° is perpendicular to Γ–M, Γ–M' and Γ–M'' paths, respectively, where in-plane mirror symmetry is conserved. Fig. 4(c) shows that the global band gap (highlighted by the green curve) of monolayer GdCl in the entire Brillouin zone can be manipulated between 9.8 meV and 30.3 meV by continuously rotating the in-plane magnetization. The band gap reaches the maximum along $\theta = 30°$, 90°, 150°, 210°, 270° and 330°, where the in-plane magnetization direction is perpendicular the Γ–K path. The band gap of monolayer GdCl is larger than that of monolayer LaCl (4 meV),[27] due to the larger SOC effect in GdX systems. The global band gaps of other monolayer GdX are listed in Table 1.

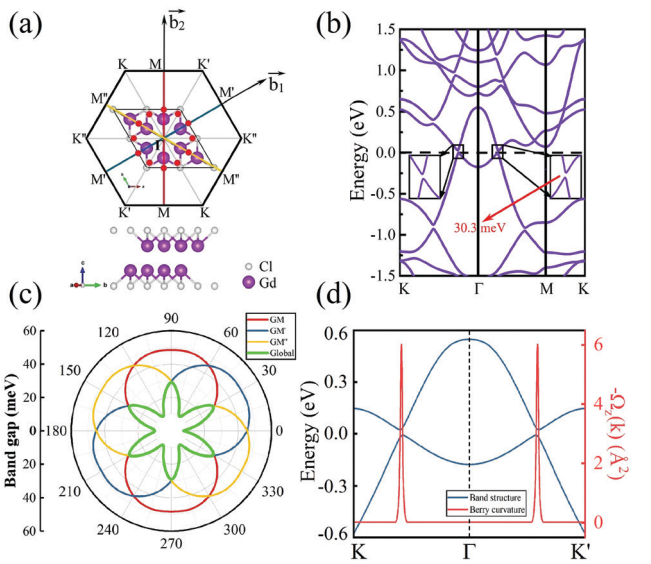

Fig. 4 QAHE in monolayer GdX. (a) The 2D Brillouin zone of monolayer GdCl. The three mirror planes are along the Γ–M, Γ–M' and Γ–M'' paths. Red dots indicate the positions of twelve two-fold degenerate band crossings along the nodal line. (b) The mBJ calculated band structure with SOC for in-plane magnetization along the *y* axis (θ = 90°). The band gap is 30.3 meV. (c) Manipulation of the mBJ calculated band gaps of monolayer GdCl by rotating the in-plane magnetization. The red, blue, and yellow lines represent the SOC band gaps opened along the Γ–M, Γ–M', and Γ–M'' paths, respectively. The band gap is a function of θ, satisfying the formula: gap (θ) = max × |sin(θ)| + min × |cos(θ)|, where the "max" and "min" are the maximum and minimum of 48.4 meV and 9.8 meV, respectively. The green curve represents the global band gap, in which the gap reaches the maximum of 30.3 meV at θ = 30°, 90°, 150°, 210°, 270° and 330°. (d) The band structure of monolayer GdCl along the path K-Γ–K' (blue curves) and the distribution of the corresponding Berry curvature in momentum space (red curve).

Berry curvature and edge states

The nontrivial topology of monolayer GdCl can also be identified by the Berry curvature (Chern number) calculation.[45,50] The Berry curvature $\Omega_z(k)$ of a 2D system can be obtained by analyzing the Bloch wave functions from the self-consistent potentials by the following formula:

$$\Omega_z(k) = \sum_n f_n \Omega_n^z(k) \quad (1)$$

$$\Omega_n^z(k) = -2\sum_{m\neq n} \mathrm{Im}\frac{\Psi_n(k)|v_x|\Psi_m(k)\Psi_m(k)|v_y|\Psi_n(k)}{(\varepsilon_m(k)-\varepsilon_n(k))^2} \quad (2)$$

where f_n is the Fermi–Dirac distribution function, $\nu_{x(y)}$ is the velocity operator, $\Psi_n(k)$ is the Bloch wave function, and $\varepsilon_{n(m)}(k)$ represents the eigenvalue. The summation is over all n occupied bands below the Fermi level and m unoccupied bands above the Fermi level. The Berry curvature $\Omega_z(k)$ is calculated by Wannier interpolation, which uses Wannier90 to perform a gauge transformation between the Bloch functions and the real space Wannier function.[51,52]

The Chern number is obtained by integrating the Berry curvature $\Omega_z(k)$ over the Brillouin zone:

$$C = \frac{1}{2\pi}\int d^2k\Omega_z(k) \quad (3)$$

Based on the Berry curvature analysis (Fig. 4(d)), we find that the Chern number of monolayer GdCl periodically changes between +1 and −1 on the interval of 60°, *i.e.* the Chern numbers along θ = 30°/150°/270° and θ = 90°/210°/330° have an opposite sign, which is determined by the orientation of in-plane magnetization. A similar scenario has been reported in monolayer LaCl[27] and alkaline metal monochalcogenide.[53] The non-zero Chern number characterizes the QAHE with the in-plane magnetization of monolayer GdCl. Additionally, the corresponding 1D topological edge state is shown in Fig. S4 in the ESI.† Within the energy window of the SOC gap, each edge has one edge state connecting the valence and conduction band, demonstrating the characterized feature of QAHE. Two edge

states cross at point Γ, which is protected by time-reversal symmetry and original lattice translation.

Magnetic field- and strain-tunable quantum anomalous Hall effect

We notice that the magnetic anisotropic energy of GdX is small (around 0.1 meV), suggesting that the external magnetic field can be used to realize the QAHE with out-of-plane magnetization. The global band gaps of monolayer GdX for out-of-plane magnetization are listed in Table 1. Monolayer GdI has the largest band gap of 84.3 meV in all halides considered in this work. In addition, we consider the strain effect in monolayer GdX. Interestingly, we find that the band gap of monolayer GdX displays different trends under the biaxial strain along x and y directions, *e.g.* the band gap of GdF and GdCl increases, while the band gap of GdBr and GdI decreases as the applied strain increases, as shown in Fig. S5 in the ESI.† Considering the strain does not break the mirror symmetry, the QAHE can be maintained. The magnetic moments of GdX under different strain are shown in Fig. S5 in the ESI.†

Curie temperature T_C

We evaluate the T_C of monolayer GdX by Monte Carlo simulations based on the Heisenberg and anisotropy exchange model. Considering the nearest, second, and third neighbor coupling of on-site spin, the Hamiltonian[54,55] can be written as:

$$\boldsymbol{H} = -2J_1\sum_{\langle i,j\rangle}\boldsymbol{S}_i\cdot\boldsymbol{S}_j - 2J_2\sum_{\langle\langle i,j\rangle\rangle}\boldsymbol{S}_i\cdot\boldsymbol{S}_j - 2J_3\sum_{\langle\langle\langle i,j\rangle\rangle\rangle}\boldsymbol{S}_i\cdot\boldsymbol{S}_j - D\sum_i\left|\boldsymbol{S}_i^z\right|^2 - 2\lambda\sum_{\langle i,j\rangle}\boldsymbol{S}_i^z\cdot\boldsymbol{S}_j^z \quad (4)$$

where $\langle i,j\rangle$, $\langle\langle i,j\rangle\rangle$, and $\langle\langle\langle i,j\rangle\rangle\rangle$ denote the nearest, second, and third neighbor spins. $J_{1,2,3}$ are the corresponding Heisenberg exchange constants. D and λ represent single ion anisotropy and anisotropic symmetric exchange, respectively. Refer to Table S6 in the ESI† for more calculation details of T_C. The predicted T_C for monolayer GdX (510–650 K) are above room temperature (listed in Table 1), much higher than that of monolayer LaCl ($\sim$260 K).[56] This shows a great potential to realize high temperature QAHE experimentally for practical applications.

Conclusions

In this study, we predict a new class of 2D electrides GdX (X = F, Cl, Br, and I), whose monolayer structures are good candidates for realizing a large-gap QAHE. Our calculations demonstrate that the spin-polarized interstitial electrons between Gd^{3+} sheets play an important role in stabilizing the electride crystal structure and contribute to ferromagnetism. We unveil that monolayer GdX is a real material for realizing the intrinsic QAHE with in-plane magnetization, which has only been reported in monolayer LaCl. With the large SOC band gaps up to 48.6 meV, and high Curie temperatures of 510–650 K, monolayer GdX has great potential to enable the practical application of high-temperature quantum devices. Moreover, larger band gaps can be obtained in monolayer GdX by applying an external magnetic field and strain engineering. Overall, our work shows the value of exploring novel topological phases in electride systems.

Conflicts of interest

There are no conflicts to declare.

Acknowledgements

This work was supported by the National Natural Science Foundation of China (Grants No. 51861145315, 11929401 and 12074241), the Independent Research and Development Project of State Key Laboratory of Advanced Special Steel, Shanghai Key Laboratory of Advanced Ferrometallurgy, Shanghai University (SKLASS 2020-Z07) and the Science and Technology Commission of Shanghai Municipality (Grants No. 19010500500, 19DZ2270200 and 20501130600). C. C. and L. F. are grateful for the support from the China Scholarship Council (CSC). C. C. would also like to thank Professor Matthias Scheffler and Christian Carbogno from the Fritz Haber Institute of the Max Planck Society in Germany for their pertinent comments and suggestions.

Notes and references

1 J. L. Dye, *Nature*, 1993, **365**, 10–11.
2 P. V. Sushko, A. L. Shluger, K. Hayashi, M. Hirano and H. Hosono, *Phys. Rev. Lett.*, 2003, **91**, 126401.
3 C. Liu, S. A. Nikolaev, W. Ren and L. A. Burton, *J. Mater. Chem. C*, 2020, **8**, 10551–10567.
4 S. Matsuishi, Y. Toda, M. Miyakawa, K. Hayashi, T. Kamiya, M. Hirano, I. Tanaka and H. Hosono, *Science*, 2003, **301**, 626–629.
5 K. Lee, S. W. Kim, Y. Toda, S. Matsuishi and H. Hosono, *Nature*, 2013, **494**, 336–340.
6 Y. Zhang, H. Wang, Y. Wang, L. Zhang and Y. Ma, *Phys. Rev. X*, 2017, **7**, 011017.
7 P. Chanhom, K. E. Fritz, L. A. Burton, J. Kloppenburg, Y. Filinchuk, A. Senyshyn, M. Wang, Z. Feng, N. Insin, J. Suntivich and G. Hautier, *J. Am. Chem. Soc.*, 2019, **141**, 10595–10598.
8 S. Y. Lee, J. Y. Hwang, J. Park, C. N. Nandadasa, Y. Kim, J. Bang, K. Lee, K. H. Lee, Y. Zhang, Y. Ma, H. Hosono, Y. H. Lee, S. G. Kim and S. W. Kim, *Nat. Commun.*, 2020, **11**, 1526.
9 Y. Toda, S. Matsuishi, K. Hayashi, K. Ueda, T. Kamiya, M. Hirano and H. Hosono, *Adv. Mater.*, 2004, **16**, 685–689.
10 M. Kitano, Y. Inoue, Y. Yamazaki, F. Hayashi, S. Kanbara, S. Matsuishi, T. Yokoyama, S. W. Kim, M. Hara and H. Hosono, *Nat. Chem.*, 2012, **4**, 934–940.
11 M. Miyakawa, S. W. Kim, M. Hirano, Y. Kohama, H. Kawaji, T. Atake, H. Ikegami, K. Kono and H. Hosono, *J. Am. Chem. Soc.*, 2007, **129**, 7270–7271.
12 H. Hosono, S. W. Kim, S. Matsuishi, S. Tanaka, A. Miyake, T. Kagayama and K. Shimizu, *Philos. Trans. R. Soc. A-Math. Phys. Eng. Sci.*, 2015, **373**, 20140450.

13 M. Hirayama, S. Matsuishi, H. Hosono and S. Murakami, *Phys. Rev. X*, 2018, **8**, 031067.
14 C. Park, S. W. Kim and M. Yoon, *Phys. Rev. Lett.*, 2018, **120**, 026401.
15 B. Bradlyn, L. Elcoro, J. Cano, M. G. Vergniory, Z. Wang, C. Felser, M. I. Aroyo and B. A. Bernevig, *Nature*, 2017, **547**, 298–305.
16 H. C. Po, A. Vishwanath and H. Watanabe, *Nat. Commun.*, 2017, **8**, 50.
17 S. Zhu, L. Wang, J. Qu, J. Wang, T. Frolov, X. Chen and Q. Zhu, *Phys. Rev. Mater.*, 2019, **3**, 024205.
18 F. D. M. Haldane, *Phys. Rev. Lett.*, 1988, **61**, 2015–2018.
19 C. Liu, X. Qi, X. Dai, Z. Fang and S. Zhang, *Phys. Rev. Lett.*, 2008, **101**, 146802.
20 Y. Yao, L. Kleinman, A. H. MacDonald, J. Sinova, T. Jungwirth, D. Wang, E. Wang and Q. Niu, *Phys. Rev. Lett.*, 2004, **92**, 037204.
21 R. Yu, W. Zhang, H. Zhang, S. Zhang, X. Dai and Z. Fang, *Science*, 2010, **329**, 61–64.
22 M. Serlin, C. L. Tschirhart, H. Polshyn, Y. Zhang, J. Zhu, K. Watanabe, T. Taniguchi, L. Balents and A. F. Young, *Science*, 2020, **367**, 900–903.
23 C. Chang, J. Zhang, X. Feng, J. Shen, Z. Zhang, M. Guo, K. Li, Y. Ou, P. Wei, L. Wang, Z. Ji, Y. Feng, S. Ji, X. Chen, J. Jia, X. Dai, Z. Fang, S. Zhang, K. He, Y. Wang, L. Lu, X. Ma and Q. Xue, *Science*, 2013, **340**, 167–170.
24 K. von Klitzing, *Rev. Mod. Phys.*, 1986, **58**, 519–531.
25 J. Henk, M. Flieger, I. V. Maznichenko, I. Mertig, A. Ernst, S. V. Eremeev and E. V. Chulkov, *Phys. Rev. Lett.*, 2012, **109**, 076801.
26 Y. Ren, J. Zeng, X. Deng, F. Yang, H. Pan and Z. Qiao, *Phys. Rev. B*, 2016, **94**, 085411.
27 Z. Liu, G. Zhao, B. Liu, Z. F. Wang, J. Yang and F. Liu, *Phys. Rev. Lett.*, 2018, **121**, 246401.
28 S. Nie, H. Weng and F. B. Prinz, *Phys. Rev. B*, 2019, **99**, 035125.
29 T. Hirahara, S. V. Eremeev, T. Shirasawa, Y. Okuyama, T. Kubo, R. Nakanishi, R. Akiyama, A. Takayama, T. Hajiri, S. I. Ideta, M. Matsunami, K. Sumida, K. Miyamoto, Y. Takagi, K. Tanaka, T. Okuda, T. Yokoyama, S. I. Kimura, S. Hasegawa and E. V. Chulkov, *Nano Lett.*, 2017, **17**, 3493–3500.
30 H. Zhang, C. Lazo, S. Blügel, S. Heinze and Y. Mokrousov, *Phys. Rev. Lett.*, 2012, **108**, 056802.
31 S. Qi, Z. Qiao, X. Deng, E. D. Cubuk, H. Chen, W. Zhu, E. Kaxiras, S. B. Zhang, X. Xu and Z. Zhang, *Phys. Rev. Lett.*, 2016, **117**, 056804.
32 J. Hafner, *J. Comput. Chem.*, 2008, **29**, 2044–2078.
33 S. Grimme, *J. Comput. Chem.*, 2004, **25**, 1463–1473.
34 P. E. Blöchl, *Phys. Rev. B: Condens. Matter Mater. Phys.*, 1994, **50**, 17953–17979.
35 J. Klimeš, D. R. Bowler and A. Michaelides, *Phys. Rev. B: Condens. Matter Mater. Phys.*, 2011, **83**, 195131.
36 A. D. Becke and E. R. Johnson, *J. Chem. Phys.*, 2006, **124**, 221101.
37 V. Blum, R. Gehrke, F. Hanke, P. Havu, V. Havu, X. Ren, K. Reuter and M. Scheffler, *Comput. Phys. Commun.*, 2009, **180**, 2175–2196.
38 A. Togo and I. Tanaka, *Scr. Mater.*, 2015, **108**, 1–5.
39 F. Knoop, M. Scheffler and C. Carbogno, *J. Open Sou. Softw.*, 2020, **5**, 2671.
40 N. Metropolis and S. Ulam, *J. Am. Stat. Assoc.*, 1949, **44**, 335–341.
41 A. Simon, H. Mattausch and N. Holzer, *Angew. Chem., Int. Ed. Engl.*, 1976, **15**, 624–625.
42 H. Mattausch, A. Simon, N. Holzer and R. Eger, *Z. Anorg. Allg. Chem.*, 1980, **466**, 7–22.
43 R. E. Araujo and J. D. Corbett, *Inorg. Chem.*, 1981, **20**, 3082–3086.
44 K. Dolui, S. Ray and T. Das, *Phys. Rev. B: Condens. Matter Mater. Phys.*, 2015, **92**, 205133.
45 M. Wu, *2D Mater.*, 2017, **4**, 021014.
46 J. H. Jung, C. H. Park and J. Ihm, *Nano Lett.*, 2018, **18**, 2759–2765.
47 E. C. Stoner, *Proc. R. Soc. A*, 1939, **169**, 339–371.
48 C. J. Pickard and R. J. Needs, *Phys. Rev. Lett.*, 2011, **107**, 087201.
49 T. Inoshita, N. Hamada and H. Hosono, *Phys. Rev. B: Condens. Matter Mater. Phys.*, 2015, **92**, 201109.
50 X. Kong, L. Li, O. Leenaerts, W. Wang, X. Liu and F. M. Peeters, *Nanoscale*, 2018, **10**, 8153–8161.
51 X. Wang, J. R. Yates, I. Souza and D. Vanderbilt, *Phys. Rev. B: Condens. Matter Mater. Phys.*, 2006, **74**, 195118.
52 A. A. Mostofi, J. R. Yates, Y. S. Lee, I. Souza, D. Vanderbilt and N. Marzari, *Comput. Phys. Commun.*, 2008, **178**, 685–699.
53 X. Zhou, R. Zhang, Z. Zhang, D. Ma, W. Feng, Y. Mokrousov and Y. Yao, *J. Phys. Chem. Lett.*, 2019, **10**, 3101–3108.
54 N. Sivadas, M. W. Daniels, R. H. Swendsen, S. Okamoto and D. Xiao, *Phys. Rev. B: Condens. Matter Mater. Phys.*, 2015, **91**, 235425.
55 J. L. Lado and J. Fernández-Rossier, *2D Mater.*, 2017, **4**, 035002.
56 Z. Jiang, P. Wang, J. Xing, X. Jiang and J. Zhao, *ACS Appl. Mater. Interfaces*, 2018, **10**, 39032–39039.